An improved derivation of the top-of-atmosphere albedo from POLDER/ADEOS-2: Narrowband albedos

Jean-Claude Buriez, Frédéric Parol, Céline Cornet, Marie Doutriaux-Boucher

An improved derivation of the top-of-atmosphere albedo from POLDER/ADEOS-2: Narrowband albedos

Jean-Claude Buriez, Frédéric Parol, Céline Cornet, and Marie Doutriaux-Boucher

Laboratoire d'Optique Atmosphérique UMR CNRS 8518, Université des Sciences et Technologies de Lille, Villeneuve d'Ascq, France

Received 16 July 2004; revised 18 November 2004; accepted 15 December 2004; published 4 March 2005.

[1] The Polarization and Directionality of Earth Reflectances (POLDER) instrument was routinely functioning aboard the second Advanced Earth Observing Satellite (ADEOS-2) from April to October 2003. A series of algorithms dedicated to Earth radiation budget, water vapor, and clouds are applied to the POLDER data. This paper presents the derivation scheme of the narrowband albedos at the top of the atmosphere from POLDER measurements at 443, 670, and 865 nm. These narrowband albedos are used to estimate the broadband shortwave albedo at the top of atmosphere in a companion paper. Here we focus on the 670 nm (over land)/865 nm (over ocean) albedo. Although our derivation is based on the plane-parallel hypothesis, and thanks to the multidirectional capability of POLDER, results appear reliable for both cloudy and clear-sky scenes. A quality index is introduced from the comparison between the angular variability of the retrieved "directional" albedo values and that of the measured reflectances. This quality index is "good" in 80% of the cases. Moreover, the retrieved albedo values are found to be statistically little dependent on the viewing direction.

Citation: Buriez, J.-C., F. Parol, C. Cornet, and M. Doutriaux-Boucher (2005), An improved derivation of the top-of-atmosphere albedo from POLDER/ADEOS-2: Narrowband albedos, *J. Geophys. Res.*, *110*, D05202, doi:10.1029/2004JD005243.

1. Introduction

[2] One of the major weakness in current climate models lies in the impact of clouds upon the radiative energy flow through the Earth-atmosphere system. As a consequence, there is a need for accurate global observations of top-of-atmosphere (TOA) radiative flux combined with coincident cloud and aerosol properties [*Wielicki et al.*, 1995]. Global cloud and aerosol properties are routinely retrieved from measurements of multichannel narrowband radiometers such as the imagers aboard weather satellites (see for instance the International Satellite Cloud Climatology Project (ISCCP) [*Rossow and Schiffer*, 1999] and more recently the Moderate Resolution Imaging Spectroradiometer (MODIS) [*Barnes et al.*, 1998]). On the other hand, TOA shortwave and longwave fluxes are usually obtained from broadband radiometers such as the Earth Radiation Budget Experiment (ERBE) [*Barkstrom et al.*, 1989], the Scanner for Radiation Budget (ScaRaB) [*Kandel et al.*, 1998] and now the Clouds and the Earth's Radiant Energy System (CERES) [*Wielicki et al.*, 1998].

[3] The Polarization and Directionality of Earth Reflectances (POLDER) instruments [*Deschamps et al.*, 1994] were launched onboard the Advanced Earth Observing Satellites (ADEOS-1 and ADEOS-2) in August 1996 and December 2002, respectively. These instruments present the particularity of having multispectral, multipolarization and multidirectional capabilities. They allow to retrieve cloud properties such as cloud fraction, optical thickness, pressure, phase, etc. [*Parol et al.*, 1999], aerosol properties such as aerosol optical thickness and Angström coefficient [*Deuzé et al.*, 2000], ocean color [*Fougnie et al.*, 1999] and land surface properties [*Hautecoeur and Leroy*, 1998].

[4] Moreover, improved estimates of TOA albedo can be expected from POLDER multidirectional measurements. To derive the albedo from bidirectional reflectance observations, or equivalently, the hemispherical flux from radiance observations, several approaches are possible. In the usual method, the radiance is converted in flux by using a set of angular distribution models (ADMs), that are constructed on a statistical basis in a more or less refined way [*Suttles et al.*, 1988; *Loeb et al.*, 2003]. *Loeb et al.* [2000] showed that POLDER observations can be very useful for building ADMs. Another approach is based on radiative transfer modeling. This technique has been used for estimating fluxes from ISCCP cloud properties [*Zhang et al.*, 1995; *Rossow and Zhang*, 1995]. This second approach is used in this study. In a first step, the narrowband albedos are derived from bidirectional reflectances by using a radiative transfer model. These retrievals are performed at 443, 670, and 865 nm. We will focus on the values retrieved at 670 nm over land and at 865 nm over ocean. In a second step, all the three narrowband albedos are used to estimate the broad-

0148-0227/05/2004JD005243

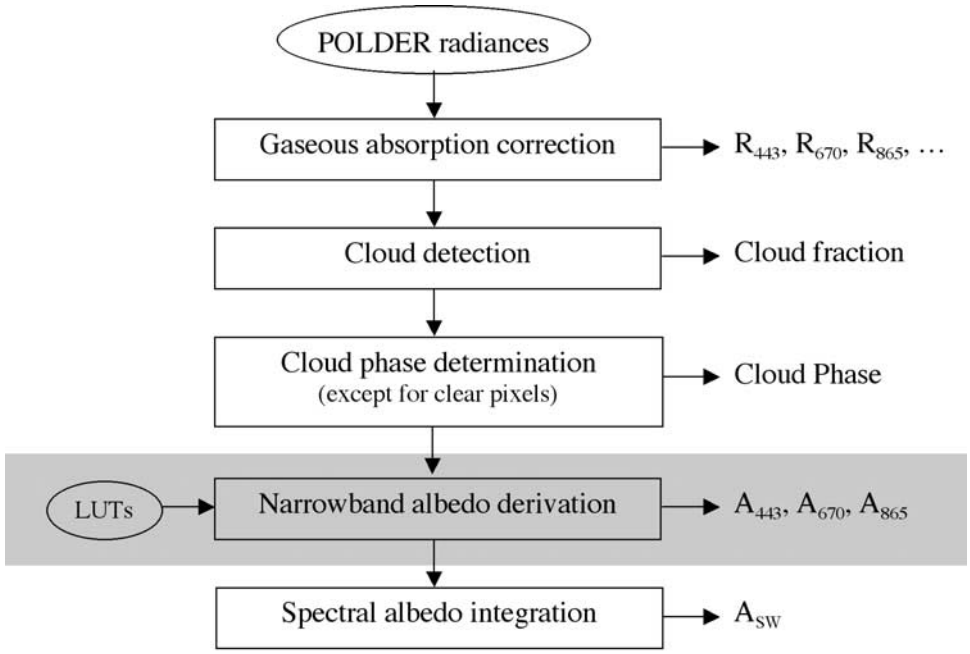

Figure 1. Diagram of the POLDER "ERB, water vapor, and clouds" level 2 processing line (ERB is Earth Radiation Budget). Only the part useful for the derivation of narrowband and broadband albedos is reported here. Object of the present paper is shaded in gray.

band shortwave albedo. This second point is described in a companion paper (J. C. Buriez et al., An improved derivation of the top-of-atmosphere albedo from POLDER/ADEOS-2. Part II: Broadband albedo, manuscript in preparation, 2005, hereinafter referred to as Buriez et al., manuscript in preparation, 2005).

[5] Our method is close to a previous one described by *Buriez et al.* [1997] (hereafter referenced as B97) and applied to POLDER-1 observations [*Parol et al.*, 1999]. As the POLDER instrument observes a given scene under up to 14 viewing directions, the albedo is estimated from each viewing direction. Ideally the retrieved values of albedo should be the same whatever the viewing direction is. However, large differences between different "directional" values of albedo were observed notably because of two major limitations linked respectively to the previous microphysical model [*Doutriaux-Boucher et al.*, 2000] and to the plane-parallel assumption [*Buriez et al.*, 2001]. These defaults are now reduced.

[6] A short description of the whole POLDER data processing is reported in section 2. The method of derivation of the narrowband albedos is described in section 3 for cloudy pixels and in section 4 for clear pixels. The albedo values derived for each viewing direction are then weighted averaged and a quality index is introduced in section 5. Results are given in section 6 and the conclusions are drawn in section 7.

2. POLDER "ERB, Water Vapor, and Clouds" Processing Line

[7] The first POLDER instrument functioned nominally aboard ADEOS from November 1996 to June 1997. The second POLDER instrument, identical to the first one, was functioning continuously aboard ADEOS-2 from April 2003 to October 2003. The orbits of both the satellite ADEOS and ADEOS-2 were Sun-synchronous with an equatorial crossing time of 10:30 local time.

[8] POLDER is a camera composed of a wide field-of-view telecentric optics, a rotating wheel carrying spectral filters and polarizers, and a coupled device detector (CDD) array of 242 × 274 detectors that induces a spatial resolution of 6.2 km. As the satellite moves over a region, up to 14 successive measurements are acquired in eight narrow spectral bands located between 443 and 910 nm. The POLDER level 1 products routinely processed by CNES (the French space agency) consist of calibrated radiances and Stokes parameters at full spatial resolution. The level 2 and 3 products are split into different lines which are "Ocean Color," "Land Surfaces," "Aerosols," and "ERB, water vapor, and clouds." The derivation of the albedo under consideration is a part of the latter processing line. Note that POLDER level 2 and 3 products correspond to about 20 × 20 km^2 "superpixel" regions, composed of 3 × 3 full-resolution pixels instead of 9 × 9 in B97.

[9] The diagram reported in Figure 1 corresponds to the part of the algorithm used for the derivation of narrowband and broadband albedos. First, the POLDER measurements in channels centered at 443, 670, and 865 nm that are weakly affected by gaseous absorption are converted in reflectances corrected from gaseous absorption. Then a cloud fraction (at the 3 × 3 pixel resolution) is determined by applying a cloud detection algorithm to each full-resolution POLDER pixel and direction. The cloud detection scheme consists of a sequence of threshold tests chiefly based on the ratio of 763- and 765-nm channel reflectances, the reflectance R(865 nm over ocean, 443 nm over land), the 443- and 865-nm polarized reflectances, and the ratio of

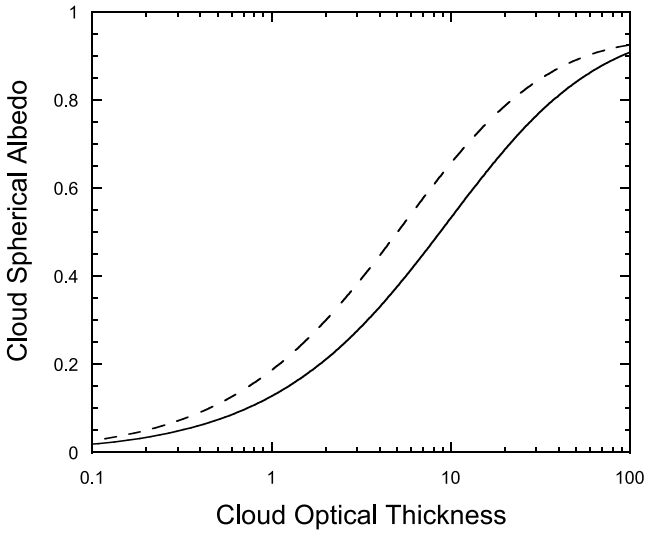

Figure 2. Examples of relationship between cloud spherical albedo and cloud optical thickness. Solid curve corresponds to a liquid water cloud layer composed of droplets with an effective radius of 11 μm. Dashed curve corresponds to an ice cloud layer composed of inhomogeneous hexagonal crystals. Wavelength is λ = 865 nm.

443- and 865-nm reflectances [*Sèze et al.*, 1999]. Cloud thermodynamic phase is derived from polarized reflectance at 865 nm [*Riédi et al.*, 2001]. Narrowband albedos $A(\lambda$ = 443, 670 and 865 nm) are then derived by using a look-up table (LUT) technique described in the next part of this paper. Finally, these albedos are combined to estimate the broadband shortwave albedo (see the second part of this series). Note that our algorithm is not applied to surfaces that could be snow covered or iced according to ECMWF (European Centre for Medium-Range Weather Forecasts) analysis since the retrieved parameters would be too doubtful in these cases.

3. Method of Derivation of Albedo for Cloudy Pixels

3.1. LUT Building

[10] In a preliminary step, modeled reflectance and albedo LUTs are built. The TOA bidirectional reflectances (R) and the associated albedos (A) are calculated by using a plane-parallel radiative transfer model. This model is a modified version of *de Haan et al.*'s [1987] adding-doubling code. These tables of reflectances and albedos are built for three wavelengths (443, 670 and 875 nm), two surface types (land and ocean) and two cloud types (ice and liquid water). They correspond to 33 values of cosine of solar zenith angle $\mu_s = \cos\theta_s$, 20 values of cloud spherical albedo S_c and 10 values of surface albedo for land surface type, with in addition for the reflectance LUTs, 28 values of cosine of viewing zenith angle $\mu_v = \cos\theta_v$ and 37 values of relative azimuth angle φ. The different nodal points have been chosen in order to provide a good interpolation accuracy ($\Delta S_c < 0.002$). Note that the spherical (or diffuse) albedo S_c is defined for a plane-parallel cloud layer over a black surface with no atmosphere, and is obtained by integrating the reflectance over all viewing zenith, solar zenith, and relative azimuth angles. In other words, it represents the cloud reflectance independent of directional, surface, and atmospheric effects. Therefore it is a one-to-one function of the cloud optical thickness τ_c for a given microphysical model (see Figure 2).

[11] To built these LUTs, radiative transfer calculations are performed by considering the atmosphere model shown in Figure 3. The atmosphere is composed of molecules, aerosols and, if necessary, ice crystals or liquid water droplets. Over ocean, aerosols are assumed to be uniformly distributed over the two lowest kilometers of the atmosphere (sigma level from 0.8 to 1.0). Their characteristics are those of the maritime component derived by *Smirnov et al.* [2003] from the Aerosol Robotic Network (AERONET) observations at the Lanai site in the Pacific. The aerosol optical thickness is 0.04 at 1020 nm. The extinction efficiency factor, the scattering phase function and the single-scattering albedo were computed at 443, 670 and 865 nm by using Lorenz-Mie theory. Over land, the aerosol optical thickness is set to zero in order to be consistent with the POLDER "Land Surfaces" processing line that often assumes no aerosol for the surface parameters retrieval. This point is discussed later (see subsection 3.2).

[12] The liquid water cloud layer when present is assumed to be located between the 0.8 and 0.9 sigma levels. Ice clouds are between the 0.3 and 0.4 sigma levels. That corresponds to a geometric thickness of about one kilometer for low-level clouds and two kilometers for high-level clouds, in agreement with *Poore et al.*'s [1995] climatology. In B97, all the cloud particles were assumed to be liquid water droplets with an effective radius of 10 μm. From POLDER polarization measurements over liquid water clouds, *Bréon and Colzy* [2000] found typically an effective radius of 9 μm for continental situations and 11 μm for

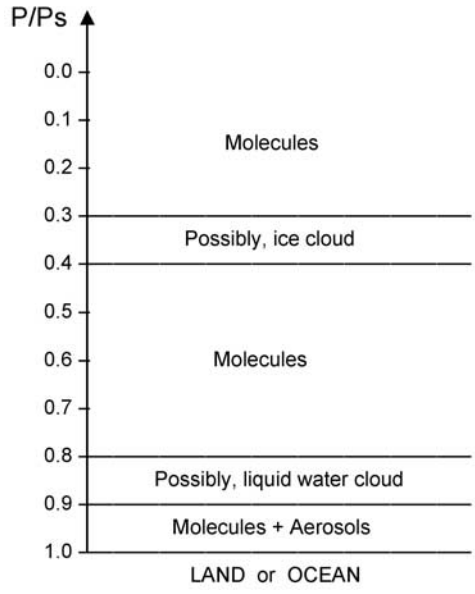

Figure 3. Model of the atmosphere used to build the look-up tables. Vertical axis represents the sigma level, i.e., the ratio between the level pressure and the surface pressure.

Table 1. Optical Properties of the Cloud Particle Models Used to Build the Look-Up Tables: Normalized Optical Thickness $\tau_c(\lambda)/\tau_c(\lambda_o)$ (λ_o = 670 nm Over Land and 865 nm Over Ocean), Coalbedo $1 - \omega_c(\lambda)$, and Asymmetry Parameter $g_c(\lambda)$

	Liquid Water Droplets (Over Ocean)			Liquid Water Droplets (Over Land)			Ice Crystals		
	λ = 443 nm	λ = 670 nm	λ = 865 nm	λ = 443 nm	λ = 670 nm	λ = 865 nm	λ = 443 nm	λ = 670 nm	λ = 865 nm
$\tau_c(\lambda)/\tau_c(\lambda_o)$	0.980	0.991	1.000	0.987	1.000	1.011	1.000	1.000	1.000
$1 - \omega_c(\lambda)$	4E-7[a]	4.0E-6	5.2E-5	3E-7	3.2E-6	4.3E-5	1.7E-6	1.2E-5	2.1E-4
$g_c(\lambda)$	0.866	0.861	0.858	0.864	0.858	0.853	0.743	0.753	0.767

[a]Read 4E-7 as 4×10^{-7}.

maritime situations, values close to those of *Han et al.* [1994]. We make use of these values for liquid water cloud droplets. For ice cloud particles, a cloud droplet model is quite inadequate [e.g., *Doutriaux-Boucher et al.*, 2000]. We use the Inhomogeneous Hexagonal Monocrystal (IHM) model developed by *C.-Labonnote et al.* [2000]. This model was found to be in very good agreement with both total and polarized reflectance measurements of POLDER [*C.-Labonnote et al.*, 2001]. It corresponds to randomly oriented hexagonal ice crystals containing air bubbles. The ice crystal length/diameter is $L/2R$ = 137 μm/55 μm while the air bubble effective radius is r_{eff} = 1 μm. The optical characteristics of the cloud particle models used to build the LUTs are reported in Table 1. The scattering phase functions were expanded in a hundred of Legendre polynomials by using the accurate procedure developed by *Hu et al.* [2000].

[13] In this LUT built-up step, the sea surface bidirectional reflectance is calculated by using the *Cox and Munk* [1956] model with a Gaussian and isotropic slope distribution for a reference wind speed V_0 = 7 m/s (see details in Appendix A). On the other hand, land-surface reflectances are taken as Lambertian. In a second step, additional anisotropy contributions due to land-surface bidirectional reflectance or actual wind vector effect on sea surface are taken into account (see subsection 3.2).

[14] As outlined by *Minnis et al.* [1998], an angular interpolation between LUT values can introduce large errors in reflectance. Whereas errors are weak for directions where the cloud phase function is smooth, they can be much too large for particular directions such as the cloudbow and the backscattering direction. As large errors due to interpolation between angle nodes are related to large angular variations in the reflectance part due to the first order of scattering R_1, only the difference $R - R_1$ is interpolated. The reflectance R_1 due to the first order of scattering is calculated for the scattering angle Θ of the observation by using the relation

$$R_1 = (\omega_c P_c(\Theta)/k_c)\exp(-m\tau_{m0})[1 - \exp(-mk_c\tau_c)]/[4(\mu_s + \mu_v)], \quad (1)$$

where ω_c and $P_c(\Theta)$ are respectively the single-scattering albedo and the scattering phase function corresponding to the cloud microphysical model; m is equal to $1/\mu_s + 1/\mu_v$; τ_{m0} is the optical thickness of the clear atmosphere above the cloud; the coefficient $k_c < 1$ that reduces the cloud optical thickness τ_c takes into account the sharp diffraction peak near 0° scattering angle: the light scattered in the narrow range of the forward direction is merged into the unscattered light [*Potter*, 1970]. The value of k_c that smoothes at best angular variations of $R - R_1$ was calculated by trial and error. Practically, the reflectance LUTs contain values of $R - R_1$ instead of R. The term R_1 given by equation (1) is then added to the interpolated values $[R - R_1]_{interp}$ in the following step (see equations (2)–(3)).

3.2. Reduced Tables of Modeled Reflectance and Albedo

[15] For a given superpixel composed of 3 × 3 pixels, reduced tables of reflectance and of albedo are derived from the above-described LUTs. For a given viewing direction, these reduced tables are only function of the cloud optical thickness τ_c (or equivalently of the cloud spherical albedo S_c) and are built in the following way: (1) The LUTs are chosen according to the surface type (land/ocean) of the superpixel and to the cloud phase (liquid/ice). For the ambiguous cases where the cloud phase is not clearly liquid or ice, the liquid water droplet model is chosen as liquid water clouds are statistically more present than ice clouds. (2) For continental cases, the values of reflectance and of albedo are linearly interpolated for the surface albedo value derived from the POLDER "Land Surfaces" level 3 processing line [*Hautecoeur and Leroy*, 1998]. Due to registration uncertainties, this surface albedo value is first averaged over all the pixels composing the superpixel. (3) The values of albedo are linearly interpolated in μ_s and the values of reflectance are multilinearly interpolated in μ_s, μ_v and φ for the viewing geometry corresponding to the observation of the superpixel. (4) Finally, the modeled values of reflectance are corrected from a surface reflectance effect and the single scattering contribution is added back, as follows:

[16] For superpixels over ocean, the sea surface reflectance $R_{surface}(\mu_s, \mu_v, \varphi, \mathbf{V})$ is calculated for the 10-m elevation wind vector $\mathbf{V}$ derived from the nearest ECMWF analysis (see Appendix A). It differs from the sea surface reflectance used in the LUTs that corresponds to a reference wind intensity V_0 = 7 m/s. The sea surface reflectance difference $R_{surface}(\mu_s, \mu_v, \varphi, \mathbf{V}) - R_{surface}(\mu_s, \mu_v, \varphi, V_0)$ can have an important effect on the light directly reflected by the surface; but it is assumed to have a negligible effect on the diffuse light scattered by the atmosphere. Consequently the modeled TOA reflectance is given by

$$R_{model}(\tau_c) = [R - R_1]_{interp}(\tau_c) + R_1(\tau_c) + [R_{surface}(\mu_s, \mu_v, \varphi, \mathbf{V}) - R_{surface}(\mu_s, \mu_v, \varphi, V_0)]\exp[-m(k_c\tau_c + k_{atm}\tau_{atm})], \quad (2)$$

where τ_{atm} is the clear-sky (molecular + aerosol) optical thickness of the oceanic atmosphere described in subsection 3.1. The coefficients k_c and k_{atm} are introduced to take into account the forward scattering peak as in equation (1).

[17] For superpixels over land, we take advantage of having not only the surface albedo $A_{surface}(\mu_s)$ but also the

bidirectional reflectance $R_{surface}(\mu_s, \mu_v, \varphi)$ derived from the surface parameters retrieved from POLDER observations by the ''Land surfaces'' level 3 processing line. For a continental superpixel, the TOA reflectance is then

$$R_{model}(\tau_c) = [R - R_1]_{interp}(\tau_c) + R_1(\tau_c) + \left[R_{surface}(\mu_s, \mu_v, \varphi) - A_{surface}(\mu_s)\right] \exp[-m(k_c\tau_c + \tau_{atm})], \quad (3)$$

where τ_{atm} is now the clear-sky (only molecular) optical thickness of the atmosphere over land ($k_{atm} = 1$ for the pure molecular scattering).

3.3. Derivation of Albedo for Cloudy Pixels

[18] For each cloudy pixel and every viewing direction, the value of the cloud optical thickness τ_c (or equivalently that of the cloud spherical albedo S_c) is obtained by inverse interpolation from the reduced table of reflectance defined in § 3.2, so that

$$R_{model}(\tau_c) = R_{measure} \quad (4)$$

where $R_{measure}$ is the POLDER reflectance corrected from gaseous absorption.

[19] Practically, the inverse interpolation is linear in cloud spherical albedo S_c rather than in optical thickness τ_c because the reflectance is much more linear in S_c than in τ_c.

[20] Then, the albedo A is derived by interpolation in the reduced table of albedo (A_{model}) for the retrieved value of S_c. This interpolation is also linear in cloud spherical albedo.

4. Method of Derivation of Albedo for Clear Pixels

[21] For clear-sky conditions, the reduced tables of modeled reflectance and albedo described in section 3.2 are limited to the case of zero cloud optical thickness ($\tau_c = 0$). Then the albedo A is estimated as described in the following subsections.

4.1. Clear Pixels Over Maritime Areas

[22] When a pixel has been classified as clear, the difference between the POLDER reflectance $R_{measure}$ and the modeled clear-sky reflectance $R_{model}(\tau_c = 0)$ is generally weak (typically within ± 0.02) but not zero. Thus the true albedo A is expected to be slightly different from the modeled clear-sky albedo $A_{model}(\tau_c = 0)$.

[23] Let us consider a cloud-free pixel over ocean. The uncertainty in the sea surface wind speed can induce a large uncertainty in the estimation of the clear-sky reflectance near the specular direction. Therefore only the observations outside the Sun glint region are used for the derivation of the albedo and the difference between the true and the modeled clear-sky albedo is assumed to be due to aerosols. Assuming a thin atmosphere over a black surface, the reflectance can be expressed as

$$R(\mu_s, \mu_v, \varphi) \equiv R_{atm}(\mu_s, \mu_v, \varphi) = [P_m(\Theta)\tau_m + \omega_a P_a(\Theta)\tau_a]/(4\mu_s\mu_v), \quad (5)$$

where $\tau_{m/a}$, $\omega_{m/a}$ and $P_{m/a}(\Theta)$ are respectively the optical thickness, the single-scattering albedo, and the scattering phase function of molecules (subscript m) and of aerosols (subscript a). One easily deduces

$$\frac{\partial A/\partial\tau_a}{\partial R/\partial\tau_a} = 4\mu_v\beta_a(\mu_s)/P_a(\Theta), \quad (6)$$

where $\beta_a(\mu_s)$ is the aerosol backscattering coefficient.

[24] Practically, for cloud-free conditions over sea, the albedo is estimated from

$$A = A_{model}(\tau_c = 0) + a(R_{measure} - R_{model}(\tau_c = 0)) \quad (7)$$

where the slope a is expressed as

$$a = \mu_v f_{sea}(\mu_s)/F_{sea}(\Theta), \quad (8)$$

where $f_{sea}(\mu_s)$ is a second-order polynomial function and $F_{sea}(\Theta)$ is a tabulated function. These functions have been fitted from radiative transfer simulations by minimizing the μ_s-weighted mean square difference between the exact value of A and the approximation given by equations (7) and (8). For these simulations, we made use of the various aerosol models described by *Dubovik et al.* [2002]. Assuming a root mean square (RMS) difference between $R_{measure}$ and $R_{model}(\tau_c = 0)$ of 0.02, we found a RMS error in albedo of 0.002–0.003 (depending on the wavelength), to be compared to about 0.01 when $a = 1$ (isotropic hypothesis) and 0.015 when $a = 0$ (no correction).

4.2. Clear Pixels Over Continental Areas

[25] For pixels over land, the problem is complicated by the effect of the surface reflectivity. First, consider that the difference between the true and the modeled clear-sky reflectance is due to aerosols. In the case of a Lambertian surface of reflectivity $R_{surface}$, equation (5) is replaced by

$$R(\mu_s, \mu_v, \varphi) = R_{atm}(\mu_s, \mu_v, \varphi) + R_{surface} \cdot T_{atm}(\mu_s)T_{atm}(\mu_v)/\left(1 - R_{surface}\, S_{atm}\right) \quad (9)$$

where $R_{atm}(\mu_s, \mu_v, \varphi)$ is the atmospheric reflectance, $T_{atm}(\mu_s)$ and $T_{atm}(\mu_v)$ are the total atmospheric transmittances along the Sun-surface-satellite paths, respectively, and S_{atm} is the atmospheric spherical albedo. In the thin-atmosphere approximation, $R_{atm}(\mu_s, \mu_v, \varphi)$ is given by equation (5), $T_{atm}(\mu_s)$, $T_{atm}(\mu_v)$ and S_{atm} are given by [e.g., *Coakley and Chylek*, 1975]

$$T_{atm}(\mu) = 1 - [\beta_m(\mu)\tau_m + (1 - \omega_a + \beta_a(\mu)\omega_a)\tau_a]/\mu \quad (10)$$

and

$$S_{atm} = 2\left(\bar{\beta}_m\tau_m + \bar{\beta}_a\omega_a\tau_a\right) \quad (11)$$

where $\bar{\beta} = \int_0^1 \beta(\mu)d\mu$ is the hemispheric backscattering coefficient.

[26] From these equations, one deduces

$$\frac{\partial A/\partial\tau_a}{\partial R/\partial\tau_a} = \frac{\beta_a(\mu_s) - \left[\beta_a(\mu_s) + \frac{1-\omega_a}{\omega_a}(1 + 2\mu_s) + 2\mu_s\bar{\beta}_a(1 - R_{surface})\right]R_{surface}}{\frac{P_a(\Theta)}{4\mu_v} - \left[\beta_a(\mu_s) + \frac{1-\omega_a}{\omega_a}\left(1 + \frac{\mu_s}{\mu_v}\right) + \beta_a(\mu_v)\frac{\mu_s}{\mu_v} - 2\mu_s\bar{\beta}_a R_{surface}\right]R_{surface}} \quad (12)$$

[27] Practically, for cloud-free conditions over land, equation (7) is used with the slope a expressed as

$$a = \frac{f_{land}(\mu_s) - \left[f_{land}(\mu_s) + p_{land}(1+2\mu_s) + q_{land}\mu_s(1-R_{surface})\right]R_{surface}}{\frac{F_{land}(\Theta)}{\mu_v} - \left[f_{land}(\mu_s) + p_{land}\left(1+\frac{\mu_s}{\mu_v}\right) + f_{land}(\mu_v)\frac{\mu_s}{\mu_v} - q_{land}\mu_s R_{surface}\right]R_{surface}} \quad (13)$$

where the coefficients p_{land} and q_{land}, the second-order polynomial function $f_{land}(\mu)$, and the tabulated function $F_{land}(\Theta)$ have been fitted from radiative transfer simulations by a least squares method. For the simulations, we have used the African savanna aerosol model from *Dubovik et al.* [2002]. Assuming a RMS difference between $R_{measure}$ and $R_{model}(\tau_c = 0)$ of 0.02, we found a RMS error in albedo at λ = 670 nm in the range 0.002–0.01 (depending on the surface reflectivity value), to be compared to about 0.01–0.02 when $a = 1$ (isotropic hypothesis) and about 0.02 when $a = 0$ (no correction). Quite similar errors were found at 443 nm and 865 nm.

[28] Since our least squares fit is based only on a biomass burning aerosol model, one can object that it is particularly inadequate for desert dust events. Indeed, simulations performed with Cape Verde aerosol model [*Dubovik et al.*, 2002] but inverted with the African savanna aerosol model often show errors in albedo almost as large as the difference between $R_{measure}$ and $R_{model}(\tau_c = 0)$. Our choice of the African savanna model is consistent with the POLDER ''Land Surfaces'' level 3 processing line. Indeed, the surface parameters which are used to estimate $R_{surface}$ in our algorithm are derived from the ''Land Surfaces'' algorithm that assumes either no aerosol or this aerosol model. The reason is that the aerosols detected from POLDER polarization measurements over land mainly correspond to biomass burning situations. The difference between $R_{measure}$ and $R_{model}(\tau_c = 0)$ is thus expected to be weak in the case of desert dust events since these desert aerosols have not been removed in the derivation of $R_{surface}$.

[29] Now, consider that the difference between the true and the modeled clear-sky reflectance is not due to aerosols, but to a difference between the true surface reflectance and that issued from the POLDER ''Land Surfaces'' processing line. It is then more reasonable to consider the atmospheric effect as negligible rather than to assume a Lambertian surface again. In these conditions, we have

$$\frac{\partial A}{\partial R} = \frac{\partial A_{surface}}{\partial R_{surface}} \quad (14)$$

If we assume that the surface anisotropy factor $\partial A_{surface}/\partial R_{surface}$ does not change when $A_{surface}$ and $R_{surface}$ change, then instead of equation (7), we simply have

$$A = A_{model}(\tau_c = 0)\frac{R_{measure}}{R_{model}(\tau_c = 0)} \quad (15)$$

[30] In practice, for cloud-free superpixels over land, two estimates of the albedo are calculated, by considering an aerosol effect (equations (7) and (13)) and, on the other hand by considering a surface effect (equation (15)). At this stage, it is important to remember that these albedo estimates are calculated for each of the about twelve directions. In the following, a quality index is defined from the angular variability of these retrieved directional albedos. The set of directional albedos that gives the best quality index is preserved. As an example, for the POLDER observations acquired on 25 June 2003 and presented in section 6, the quality index is found to be the best as often by using the aerosol correction as by using the surface correction. In other words, each of the albedo estimates is retained on average once on twice.

[31] Note that the derivation scheme of albedo for clear pixels is quite different from that developed in B97. Indeed, in the previous scheme, the estimated clear-sky albedo was only a crude modeled value, practically independent of the POLDER measurement.

5. Weighted Averaged Value of Albedo and Its Quality Index

5.1. Averaging Over Pixels and Over Directions

[32] The above-described calculations are performed for every viewing direction i and for every pixel p of the superpixel. Let be $A(p, i)$ a retrieved value of albedo. These values are first averaged over the $N_p = 3 \times 3$ pixels composing the superpixel,

$$A(i) = \frac{1}{N_p}\sum_{p=1}^{N_p} A(p,i), \quad (16)$$

then over the N_i ($\leq$14) viewing directions,

$$A = \sum_{i=1}^{N_i} w(\Theta(i))A(i) / \sum_{i=1}^{N_i} w(\Theta(i)), \quad (17)$$

where $w(\Theta(i))$ is a weighting function taking in account that some viewing directions are more favorable than others for the albedo retrieval, in clear-sky situations [e.g., *Kaufman et al.*, 1997] and in cloudy situations [e.g., *Loeb and Coakley*, 1998]. We distinguish the cloud-free, the liquid water cloudy, and the ice cloudy situations, over ocean and over land. Therefore there are six different weighting functions for each spectral channel. They are empirical functions of the scattering angle Θ, established from previous POLDER-1 data. The difference $A(\Theta) - \bar{A}$ between the albedo value retrieved in the Θ direction and the ''unweighted'' mean value were calculated for each of the superpixels observed by POLDER-1 during December 1996 and June 1997. The weighting function is the inverse of the mean square of these differences. Practically, the subartic regions were excluded from the data set because the meteorological sea-ice index used for the POLDER-1 data processing was found to present some anomalies.

[33] Figure 4 presents the weighting functions for the 865 nm channel over ocean and for the 670 nm channel over land. Similar functions were found for the other channels. The values are typically 10^3 for cloudy conditions, and 8 10^3 and 2 10^5 for clear-sky conditions respectively over land and over ocean; they correspond to RMS differences in albedo of about 0.03, 0.01 and 0.002 respectively. For liquid water clouds, the curves of $w(\Theta)$ are almost merged for the maritime and the continental situations. As expected from previous works [*Doutriaux-Boucher et al.*, 2000; *Buriez et*

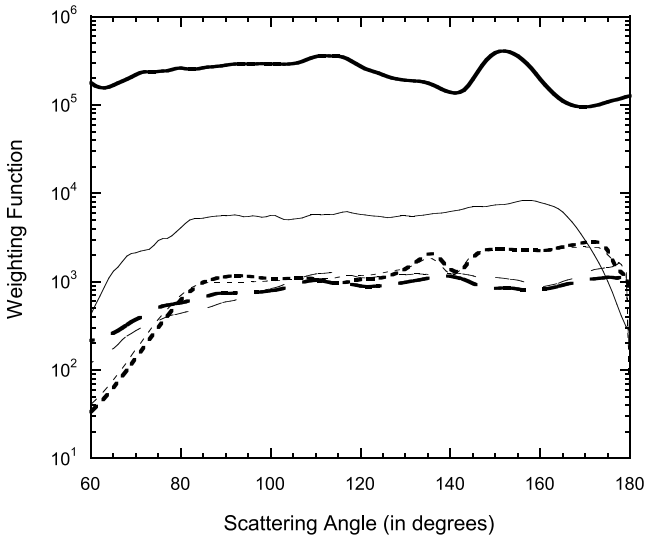

Figure 4. Weighting functions used to average the "directional" albedo values, as a function of the scattering angle. These six functions are empirically established from the ADEOS-1 POLDER observations acquired on December 1996 and June 1997, by distinguishing the cloud-free (solid curves), the liquid cloudy (dotted curves), and the ice cloudy (dashed curves) situations, over ocean (thick curves) and over land (thin curves).

al., 2001], these curves present variations near the cloudbow and the backscattering directions and a strong decrease at small scattering angles ($\Theta < 80°$). These features are thought to be related to deficiencies in the microphysical model and chiefly in the plane-parallel model [*Buriez et al.*, 2001]. In the case of ice clouds, the curves of $w(\Theta)$ are relatively smooth as expected since the complex geometric structure of the ice crystals practically leads to featureless scattering phase functions at least at large enough scattering angles [e.g., *McFarquhar et al.*, 2002]. For clear-sky situations over ocean, $w(\Theta)$ presents very small variations and always high values, that correspond to low differences between the different "directional" albedo values retrieved outside the Sun glint region. The good performance around $\Theta = 150°$ could be linked to the weak sensitivity of the aerosol phase function to the particle shape at this angle [*Mishchenko et al.*, 2003]. For clear-sky situations over land, the values of $w(\Theta)$ are relatively weak at small scattering angles, which correspond to large solar and/or viewing zenith angles, and near the backscattering direction, which corresponds to the hot spot that was not taken into account in the POLDER-1 "Land Surfaces" processing.

[34] Our choice was to weight simply the different "directional" albedos values. Another possibility would be the use of empirical corrective factors depending on the viewing geometry and the scene type. However, such an approach would be a mixture between the ADM approach and the modeling one. It seems preferable to clearly choose between the ADM method as given by *Loeb et al.* [2000] and the radiative transfer modeling. The present albedo derivation completely assumes the plane-parallel hypothesis. Such an albedo derivation, although imperfect, can be a help when compared to other completely different approaches. Here, the weighting is clearly of less importance than the averaging. Some tests with other weighting functions gave little significant differences. It is why a more complicated weighting function does not appear really useful.

5.2. Quality Index

[35] The problem is now to quantify the quality of the albedo retrieval. Ideally the retrieved values of albedo are the same whatever the viewing direction is. In order to quantify the angular variability of the retrieved directional albedo of a given superpixel, we calculate the relative angular standard deviation of the albedo

$$\frac{\sigma(A)}{A} = \frac{1}{A}\sqrt{\sum_{i=1}^{N_i} w(i)(A(i)-A)^2 / \sum_{i=1}^{N_i} w(i)}. \qquad (18)$$

[36] This relative standard deviation has to be weak but it can be weak not thanks to the quality of the retrieval but simply when the behavior of the POLDER reflectances is very similar in all the viewing directions. In this last case, the relative angular standard deviation of the measured reflectance $\sigma(R)/R$ is also weak. Therefore we define a quality index as

$$QA = \frac{1}{1+\frac{[\sigma(A)/A]}{[\sigma(R)/R]}}, \qquad (19)$$

that is equal to 1 when all is perfect and 0 in the opposite case. This quality index is equal to 0.5 when our results are neither better nor worse than that would be obtained under the Lambertian hypothesis. Note that, in very few cases, the retrieved albedo can have an unphysical value in a given direction. This value is then bounded by 0 and 1. As the above calculation has then no more meaning, the quality index is fixed to 0 for these very doubtful cases. Practically, the quality index is forced to zero in a few percent of cases that correspond to high-latitude area that are snow-contaminated and would have to be eliminated.

6. Some Results From POLDER/ADEOS

[37] The results presented in this section corresponds to the 670-nm channel over land and to the 865-nm one over ocean. These channels are chosen to illustrate the cloud effect on radiation. For maritime situations, the 865-nm channel is little sensitive to molecular and aerosol scattering. For continental situations, the 670-nm channel appears as a good compromise since it is not too affected by molecular scattering as the 443-nm channel does nor by surface reflectance as the 865-nm channel does. Very similar results are obtained with the other channels. Figure 5 shows an example of the narrowband albedos derived from the POLDER observations for the 14 ADEOS-2 orbits acquired on 25 June 2003. The values derived at high latitudes must be considered with great caution because of probable errors in the sea-ice index. In the following, we consider only latitudes lower than 60°N.

[38] A visual inspection of Figure 5 shows no abnormal discontinuity between clear scenes and scenes with very

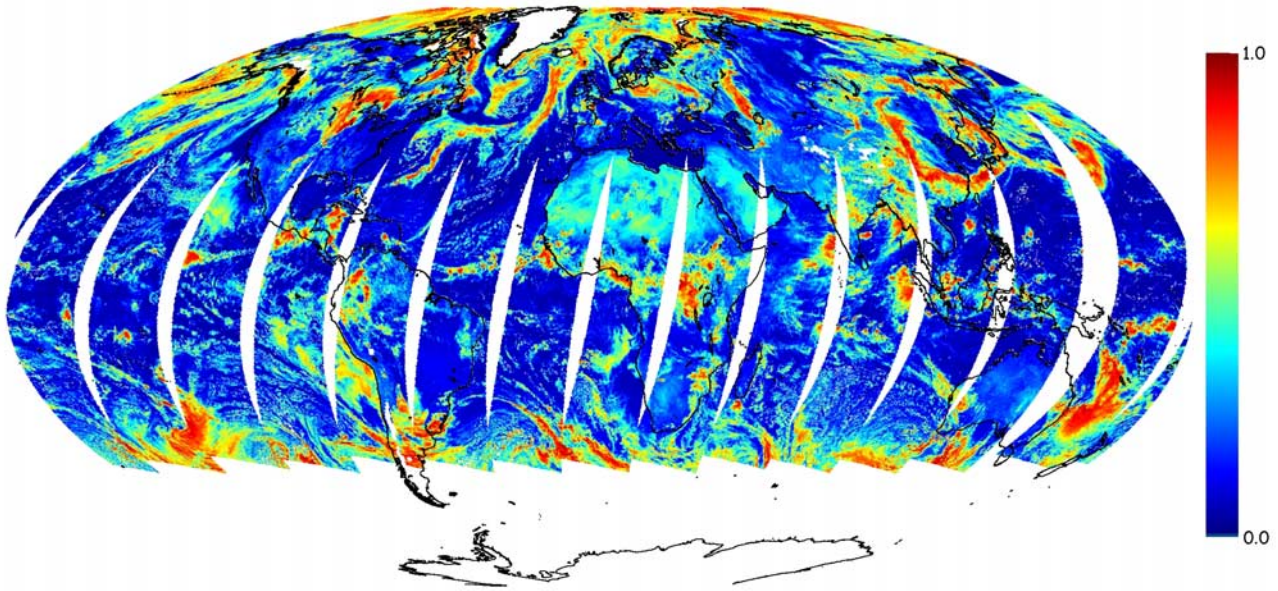

Figure 5. The 670 (over land) and 865 nm (over ocean) albedo derived from the ADEOS-2 POLDER observations on 25 June 2003.

thin and/or patchy clouds despite the distinct methodologies used to derive the albedo in clear and cloudy conditions. The variation of the mean albedo as a function of the cloud cover (CC) is reported in Figure 6. The absolute difference between the mean albedo value retrieved in clear-sky conditions and the one retrieved for very weak cloud fractions ($0 < CC < 0.1$) is weaker than 0.015 as well over land as over ocean. However, note that, over land, the TOA albedo value is not minimum for CC = 0. That can be due to physical effects such as the cloud shadowing effect and/or sampling differences between clear-sky and cloudy observations since desert areas are very bright and often cloud-free.

[39] We attempted to compare the albedo retrieved with the present scheme to that derived with the algorithm described in B97. This previous algorithm had been routinely applied by CNES to the ADEOS-1 POLDER data for the period November 1996 to June 1997. We applied the present derivation scheme to some of these data. For the 14 orbits acquired on 25 June 1997, the so derived narrowband albedo map (not shown) is overall rather similar to the previous one and also to that reported on Figure 5 for 25 June 2003 (just 6 years later). Unfortunately, a superpixel-by-superpixel comparison between previous and present retrieved albedos cannot be done because of the difference of spatial resolution. Indeed, when 9 new superpixels of about $(20\ km)^2$ are averaged (3 by 3), their area does not coincide with the one of the old superpixels of about $(60\ km)^2$. However, the latitudinal average values can be compared (see Figure 7). When averaged over half-degree latitudinal belts, the previous and the present albedo values present a RMS difference of 0.008 (3% of the mean). This difference appears all the more small because there are differences in cloud cover due to some changes in the cloud detection scheme (RMS difference of 0.02 in cloud cover). In point of fact, there are major differences that are smoothed by the zonal averaging but appear in Figure 8 where are reported the clear-sky albedos. In the B97 algorithm, the clear-sky albedo (i.e., restricted to the superpixels labeled as totally clear by the cloud detection scheme) was too crudely calculated so that its value was typically too large by 0.02–0.03 for moderate solar zenith angles when compared to expected values over ocean (N. G. Loeb, private communication, 1999). Improvements in the clear-sky albedo derivation (see section 4) can explain large differences for maritime situations and in a smaller extend for continental situations.

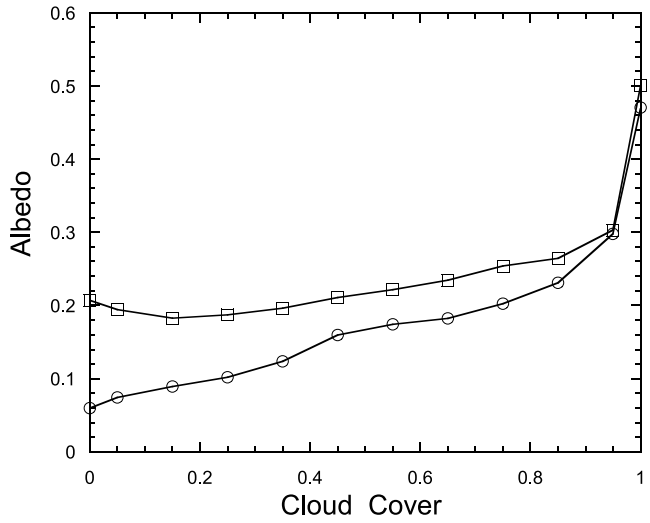

Figure 6. Variation of the albedo as a function of the cloud cover from ADEOS-2 POLDER observations on 25 June 2003. Circles (squares) correspond to the mean albedo values retrieved over ocean (land) between 60°N and 60°S, at λ = 865 nm (670 nm), for 12 classes of cloud cover: 0 (clear-sky), 0.01–0.10, 0.10–0.20, . . ., 0.80–0.90, 0.90–0.99, 1 (overcast).

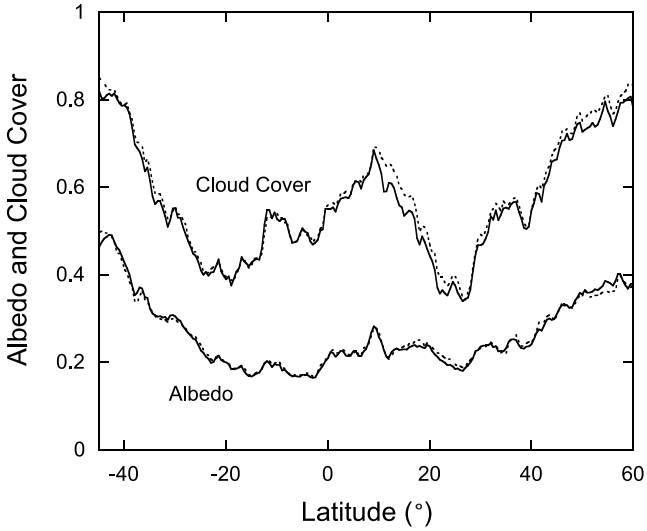

Figure 7. Latitudinal variations of the cloud cover and the albedo retrieved from ADEOS-1 POLDER observations on 25 June 1997, with the previous algorithm (dotted curves) and with the present algorithm (solid curves).

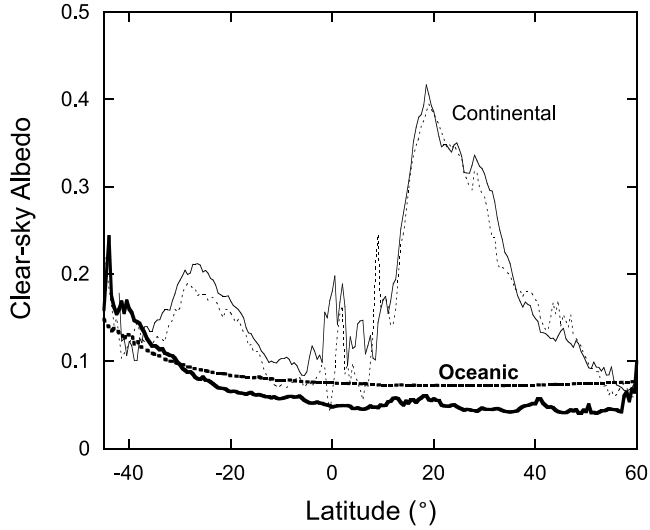

Figure 8. As in Figure 7, but for the clear-sky albedo by distinguishing between superpixels over oceans (bold curves) and over continents (thin curves).

[40] The comparison between the previous and the present algorithm was possible only for ADEOS-1 POLDER data. The ADEOS-2 POLDER data (processed only with the present algorithm) acquired on 25 June 2003 give the same latitudinal behavior (not reported) as in Figure 7 but with significant differences: the RMS difference between the 25 June 1997 and the 25 June 2003 observations is of 0.04 in albedo and 0.07 in cloud cover. These differences are due to the temporal cloudiness variability and possibly to calibration differences between POLDER-1 and POLDER-2. Note that, for POLDER-1, we used the same level 1 data as in the previous algorithm. A second set of level 1 data is presently under reprocessing by CNES in order to apply the same calibration method to POLDER-1 data as to POLDER-2 data.

[41] Concerning the cloudy-sky albedo, a major difference between the previous and the present derivation scheme concerns the microphysical model. The ice cloud particles are now assumed to be inhomogeneous hexagonal crystals while they were previously treated as liquid water droplets. In order to illustrate the impact of this modification, we ran the present algorithm by assuming the ice cloud particles are liquid water droplets as in B97. When selecting the overcast ice cloud superpixels (i.e., totally labeled as "ice" by the cloud phase scheme) observed from ADEOS-1 POLDER on 25 June 1997, we found large differences in retrieved cloud optical thickness due to the difference of microphysical model (see Figure 9). The mean ratio between liquid water-model derived and ice-model derived optical thicknesses is 1.65 for oceanic ice clouds at 865 nm and 1.73 for continental ice clouds at 670 nm. These values are quite close to the approximate values (respectively 1.64 and 1.74) deduced from similarity relations [*van de Hulst*, 1980]. On the other hand, the difference in optical thickness induces a negligible mean difference in albedo and a RMS difference of 0.027, that is 8% of the mean albedo (see Figure 10). As already noted by *Sun et al.* [2004], an algorithm that does not work well for the retrieval of cloud optical thickness, can provide satisfactory estimates of albedo. Since the liquid water model is one of the worst models for ice clouds, that gives rather confidence in the albedo derived with our crystal model.

[42] A quite important test concerns the albedo quality index *QA* that gives an idea of the performance of the albedo retrieval. The *QA* histogram is reported in Figure 11 for the whole of the POLDER observations made during June 2003. The percentage of cases for which the albedo retrieval is better than the one obtained under the Lamber-

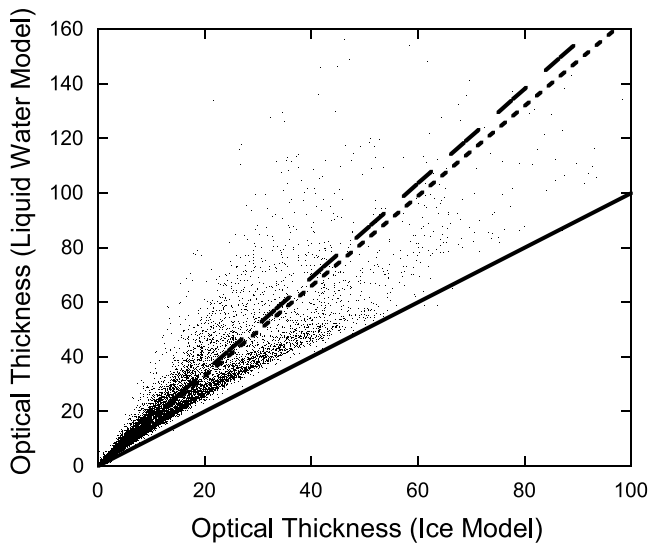

Figure 9. Comparison between the ice cloud optical thickness retrieved by using the ice crystal model and the liquid water droplet model. Comparison is restricted to the superpixels observed from ADEOS-1 POLDER on 25 June 1997 and totally labeled as "ice" by the cloud phase algorithm. Solid line is of slope unity. Short- and long-dashed lines correspond to the mean slope for the maritime and for the continental situations, respectively.

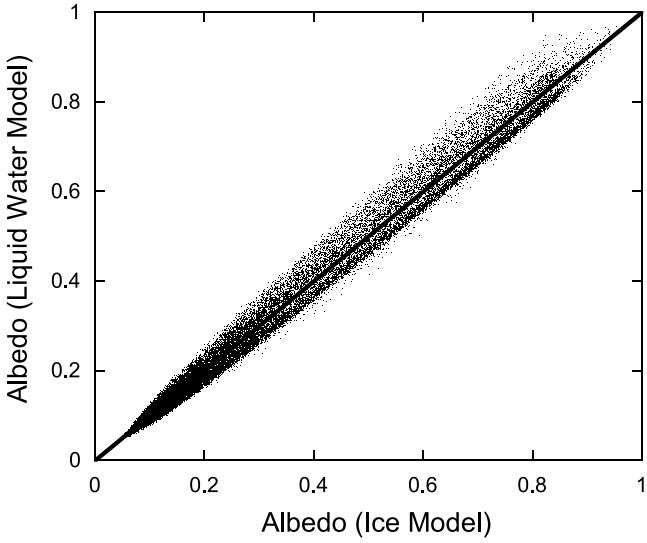

Figure 10. As in Figure 9, but for the ice cloud albedo.

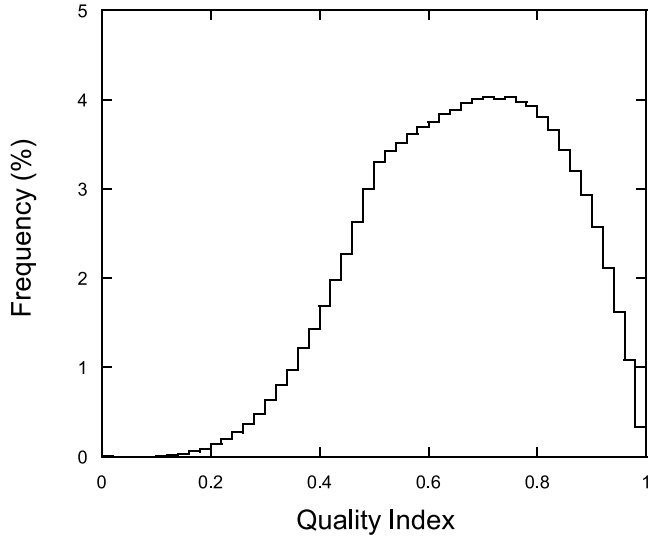

Figure 11. Histogram of the quality index for June 2003.

tian hypothesis is reported in Table 2, for all-weather, cloudy and clear-sky situations, over maritime and continental surfaces. Overall, *QA* is better than 0.5 for more than 80% of the superpixels. The quality index is better than 0.5 for 75% of the overcast superpixels. This score is better over ocean (78%) than over land (68%). That can be explained by a larger occurrence of thick stratiform cloud layers and thus more homogeneous clouds and by a less effect of the underlying surface over ocean than over land.

[43] Despite the introduction of the inhomogeneous hexagonal monocrystal model, the score appears not so good over ice clouds (69%) as over liquid water clouds (79%). This apparent poor performance is explained by the angular behavior of the ice cloud reflectance that is much smoother than the one of liquid water clouds notably in the cloudbow and the backscattering direction. Thus the angular standard deviation of the retrieved albedo has more difficulty being weaker than that of the measured reflectance for ice clouds than for liquid water clouds. Note that if ice clouds were assumed to be composed of liquid water droplets as in the previous algorithm (B97), the score would decrease from 69% to 48%.

[44] The high performance (95%) observed for clear-sky observations gives rather confidence in our clear-sky albedo retrieval. However, we have to acknowledge that it could partly result from an artifact. Indeed, if it was calculated in the previous algorithm (B97), the score would be found incorrectly equal to 100% since the clear-sky albedo was only a modeled value independent of the POLDER data and then its angular standard deviation would be inevitably zero.

[45] Finally, the score observed for partly cloudy superpixels is between the overcast and the clear-sky, but it is only 74% over land. This relative weakness can be explained by a higher difficulty in detecting cloud over land surfaces than over dark oceanic surfaces, that results in a larger uncertainty in the retrieved cloud cover and then in the retrieved albedo for continental areas.

[46] Despite the limitation related to the plane-parallel assumption, the albedo retrieval appears rather good in most cases. In order to outline the contribution of the multidirectional capability of POLDER, we compare the retrieved albedo to that would be retrieved by using only one direction. Figure 12 compares monthly means: the mean reflectance measured in a given direction, the mean albedo retrieved in that direction, and the mean albedo averaged over all the available directions. Two solar zenith angle intervals are considered: 30°–40° and 60°–70°, that correspond respectively to latitudes 15°S–10°N and 45°–65° N and latitudes 25°–50°S, for ADEOS-2 POLDER data acquired during June 2003. The viewing zenith angle intervals are 0°–5°, 5°–15°, 15°–25°, . . ., 55°–65°. Three relative azimuth angle intervals are selected: $0° < \varphi < 5°$ (forward direction), $175 < \varphi < 180°$ (backward direction), $85° < \varphi < 95°$ (side direction). For solar zenith angles of 60°–70°, there are observations beyond viewing zenith angles of 55° in the side direction but neither in the forward nor in the backward direction. In the same way, no observation is reported beyond 55° in the forward direction for solar zenith angles of 30°–40°. This is explained by the rectangular shape of the POLDER CCD matrix that does not sample all the viewing zenith and azimuth angles [see *Deschamps et al.*, 1994, Figure 3].

[47] Figures 12a and 12b show expected angular behaviors of reflectance: the weak value of ocean reflectance except in the region of solar specular reflection, the relatively large value of land surface reflectance in the backward direction and the large increase of cloud reflectance in the forward direction for low solar elevation angles.

Table 2. Percentage of Superpixels for Which the Quality Index is Better Than 0.5[a]

Conditions	All Surfaces, %	Over Ocean, %	Over Land, %
All conditions	83	85	79
Overcast clouds	75	78	68
Overcast liquid water clouds	79	82	72
Overcast ice clouds	69	71	63
Partly cloudy	83	86	74
Clear sky	95	96	95

[a]Data correspond to ADEOS-2 POLDER observations during June 2003.

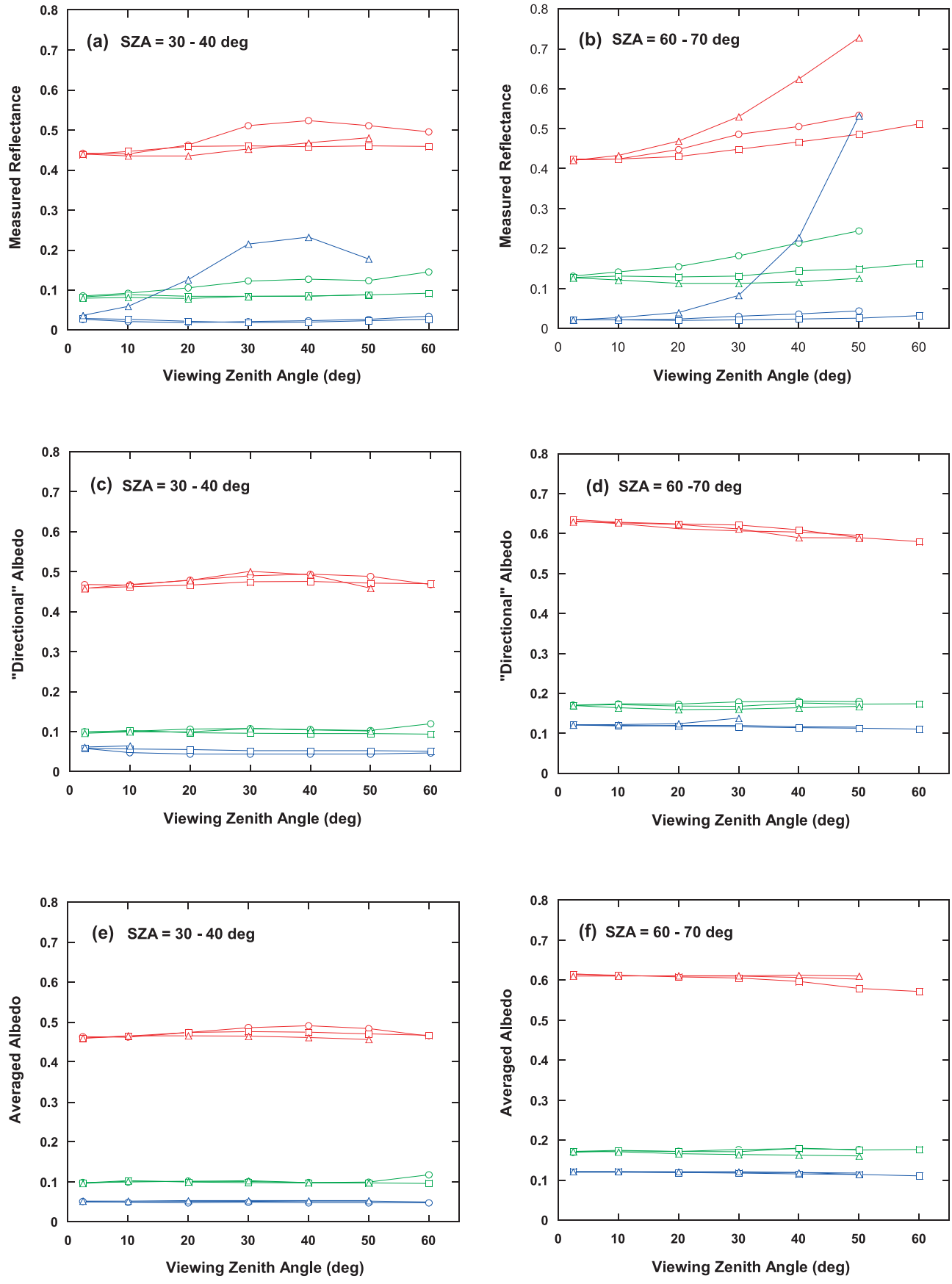
(a) SZA = 30 - 40 deg
(b) SZA = 60 - 70 deg
(c) SZA = 30 - 40 deg
(d) SZA = 60 -70 deg
(e) SZA = 30 - 40 deg
(f) SZA = 60 - 70 deg
Measured Reflectance
"Directional" Albedo
Averaged Albedo
Viewing Zenith Angle (deg)
0 0.1 0.2 0.3 0.4 0.5 0.6 0.7 0.8
0 10 20 30 40 50 60

Figure 12

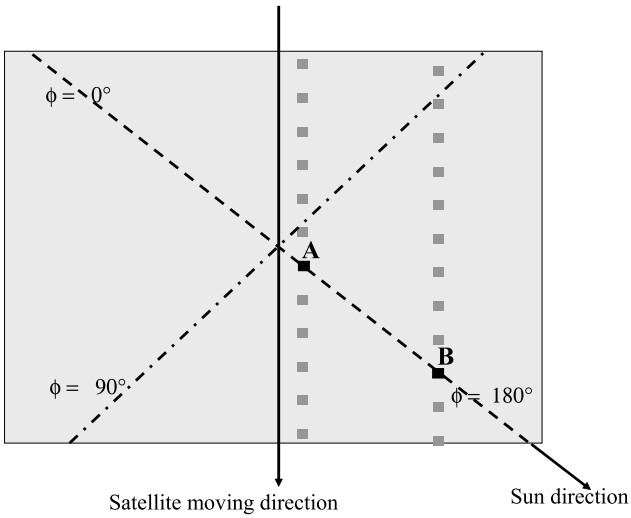

Figure 13. Schematic representation of the POLDER CCD array. Dashed line corresponds to the principal plane (φ = 0°–180°), and dash-dotted line corresponds to the cross plane (φ = 90°). Pixels A and B (black squares) correspond to two different viewing zenith angles (increasing with the distance to the matrix center), and here to the same azimuth angle φ = 180°. In the weighting averaging operation, they are associated with pixels (gray squares) that differ each from another.

[48] From the comparison between Figures 12a and 12b and 12c and 12d, our albedo retrieval is clearly proved to be much better than what would be obtained under the Lambertian hypothesis. The RMS variation in ''directional'' albedo remains close to 0.006 for clear-sky conditions both over land and over ocean, for low and high solar elevation angles. As already mentioned, the ''directional'' albedo is not calculated inside the Sun glint region over ocean. Despite this precaution, one observes a departure near the Sun glint area limits (clearly in Figure 12d for the viewing angle of 30° in the forward direction). For cloudy conditions the RMS variation in ''directional'' albedo is about twice as much as for clear-sky conditions (0.012 for 30°–40° and 0.016 for 60°–70°), that is 2.6% in relative value for both the two solar angles. For the low solar elevation case, there is a clear decrease of the ''directional'' albedo with viewing zenith angle (about 0.001 by degree). This is related to the plane-parallel cloud hypothesis.

[49] This default significantly decreases in Figure 12f where the weighted averaged albedo, that is the final result, is reported for each of the viewing directions used for the weighted averaging. Someone could wonder that the monthly mean of ''angularly averaged'' albedo still depends on the viewing direction. With a multidirectional instrument such as the Multiangle Imager Spectroradiometer (MISR) [*Diner et al.*, 1998] that uses nine discrete cameras pointed along the spacecraft ground track, the angular averaging necessarily would give values independent of the viewing direction since any target is observed under the same fixed angles. As explained in Figure 13, this is not the case with the POLDER instrument that employs a CCD array. It results that the different couples (θ_v, φ) reported in Figure 12 correspond to different geographic area and are then comparable only in a statistical way. Thus the decrease of the plane-parallel bias observed in Figure 12f is not an artifact but an improvement due to the multidirectional capability of POLDER.

7. Summary and Conclusions

[50] The POLDER instrument was routinely functioning aboard ADEOS-2 from April to October 2003. A method for deriving the TOA albedo from narrowband reflectance measurements has been developed in order to be applied to these 7-month POLDER data. It also can be applied to the earlier POLDER data acquired during the ADEOS-1 mission.

[51] The POLDER instrument observes a given scene under up to 14 viewing directions. In a first step, each viewing direction is considered separately and different ''directional'' albedo values are thus retrieved. These values are then averaged using angle-weighting functions, which are based on the statistical analysis of a large set of ADEOS-1 POLDER data.

[52] For clear pixels over ocean, we use a relation between albedo and bidirectional reflectance established from simulations of the light reflected by turbid atmospheres. Over land, we start from the estimates of surface reflectance issued from the 10-day synthesis of POLDER data produced by an operational processing line dedicated to land surfaces [*Hautecoeur and Leroy*, 1998]. Differences between the TOA reflectance calculated from these syntheses and the measured reflectance can be due to the presence of aerosols and/or the temporal variability of the surface reflectivity. In a first step, these two assumptions are considered separately and two sets of ''directional'' albedo values are derived. Then the result that gives the less angular variability for these values is preserved.

[53] For cloudy pixels, we make use of LUTs based on the plane-parallel cloud layer model. Optical properties of liquid water cloud droplets are calculated by using Lorenz-Mie theory. For ice clouds, we make use of the IHM model developed by *C.-Labonnote et al.* [2000]. If ice clouds were assumed to be composed of liquid water droplets, the retrieved albedo would differ typically by 0.03 (8% in relative value). Since the liquid water model is one of the

Figure 12. Monthly mean values of the measured reflectance, the retrieved ''directional'' albedo, and the weighted averaged albedo against viewing zenith angle. Blue corresponds to clear-sky ocean, green corresponds to clear-sky land, and red corresponds to overcast. Three relative azimuth angle intervals are selected: Triangles correspond to forward ($0° \leq \varphi \leq 5°$), circles correspond to backward ($175° \leq \varphi \leq 180°$), and squares correspond to side ($85° \leq \varphi \leq 95°$). Left and right curves correspond to solar zenith angles of 30°–40° and 60°–70°, respectively. Data corresponds to ADEOS-2 POLDER observations over June 2003. If all were perfect, the colored curves would be horizontal straight lines in Figures 12c and 12d and 12e and 12f.

worst models for ice clouds, that gives rather confidence in the albedo derived with the IHM model.

[54] We prefer to weight the different "directional" albedo values rather than to correct these values. By this way we only use a modeling approach that can be a help when compared to the ADM method that is quite different. Thus the present albedo derivation completely follows the plane-parallel hypothesis. Although the weaknesses of this hypothesis have been evidenced from simulations [*Chambers et al.*, 2001] and from observations [*Loeb and Coakley*, 1998; *Buriez et al.*, 2001], the retrieved albedo is found to be statistically little dependent on the viewing direction. This can be related to the fact that it results from an averaging over typically twelve directions. If all the possible upward directions were observed, it is evident that there would be no bias.

[55] The multidirectionality of POLDER allows us to compute a quality index that quantifies the quality of the albedo retrieval. This quality index, which derives from the comparison between the angular variability of the retrieved "directional" albedos and that of the measured reflectances, is found to be "good" in 80% of the cases. As it is calculated for each set of observations, it can be used to select cases where the albedo retrieval is most reliable.

[56] The final aim of this work is to derive the SW (shortwave) albedo from multidirectional narrowband measurements. Such a derivation from ADEOS-2 POLDER data is expected to be useful for validating or questioning the SW albedo estimates obtained from broadband radiometers such as CERES. Moreover, the derivation of the SW albedo from earlier ADEOS-1 POLDER data can be particularly useful since there was no broadband scanner in flight during the period November 1996 to June 1997. This work is the first step. The second one, which concerns the derivation of the broadband albedo from the narrowband ones, is described in the companion paper (Buriez et al., manuscript in preparation, 2005).

Appendix A: Sea Surface Reflectance Model

[57] Following *Koepke* [1984], the sea surface reflectance is expressed as

$$R_{surface}(\mu_s, \mu_v, \varphi, \mathbf{V}) = W_{foam}(V)R_{foam} + \left[1 - W_{foam}(V)\right] \cdot R_{specular}(\mu_s, \mu_v, \varphi, \mathbf{V}) + \left[1 - W_{foam}(V)R_{foam}\right].R_{underlight}, \quad \text{(A1)}$$

where $\mathbf{V}$ is the sea surface wind vector and V its intensity, W_{foam} and R_{foam} are respectively the fraction covered by whitecaps and the reflectance of the whitecaps, $R_{specular}$ is the specular reflectance at the water surface without foam and $R_{underlight}$ is the underlight reflectance due to scattering by water molecules and suspended material in the water.

[58] The fraction W_{foam} is expressed as:

$$W_{foam}(V) = 2.95\,10^{-6}\,V^{3.52}. \quad \text{(A2)}$$

R_{foam} is close to 0.22. As its value is highly uncertain, it is assumed to be independent of the wavelength though this hypothesis is dubious [*Frouin et al.*, 1996]. $R_{underlight}$ is fixed to 0.02 at 443 nm and is neglected at 670 nm and 865 nm. $R_{specular}(\mu_s, \mu_v, \varphi, \mathbf{V})$ is calculated with the Fresnel formula and the *Cox and Munk* [1956] model.

[59] In the LUTs (see section 3.1), the nondirectional Gaussian approximation of the *Cox and Munk* [1956] model is used with a reference wind intensity $V = V_0 = 7$ m/s. However, in the core of the algorithm (see equation (2)), the sea surface reflectance is calculated for the 10-m elevation wind vector $\mathbf{V}$ derived from ECMWF analysis (intensity and bearing are used in the *Cox and Munk* [1956] model).

[60] In the same way, for clear-sky conditions, the modeled albedo above ocean is calculated from the approximation:

$$A_{model}(\tau_c = 0) = p_1 + p_2 X + p_3 X^2 + p_4 X^3 + p_5 X^4 + p_6 X^5/(1 + p_7 V) + p_8 X^6/(1 + p_9 V) + \left(p_{10} + p_{11} X^3\right) V^{p_{12}}, \quad \text{(A3)}$$

where $X = 1 - \mu_s$ and the coefficients p_m ($m = 1, 12$) are derived from simulations using the modified adding-doubling code. This expression is similar to the expression of the sea surface albedo given by *Hansen et al.* [1983]. The last term is added to take into account the foam reflectance (see equations (A1) and (A2)). The coefficients p_m have been adjusted for taking into account the effect of the clear-sky atmosphere; they are thus wavelength dependent.

[61] **Acknowledgments.** The authors would like to thank P. Couvert, F. Ducos, E. Tromp and Z. Poussi for their valuable help in the algorithm development process, M. Vesperini for her modified version of the adding-doubling code, B. Bonnel and G. Brogniez for phase function calculations and Y. X. Hu for kindly providing his code. This work was funded by CNES and the Région Nord-Pas de Calais. Information on the POLDER data can be found online at http://smsc.cnes.fr/POLDER/.

References

Barkstrom, B. R., E. Harrison, G. Smith, R. Green, J. Kibler, R. Cess, and ERBE Science Team (1989), Earth Radiation Budget Experiment (ERBE) archival and April 1985 results, *Bull. Am. Meteorol. Soc.*, *70*, 1254–1262.

Barnes, W. L., T. S. Pagano, and V. V. Salomonson (1998), Prelaunch characteristics of the Moderate Resolution Imaging Spectroradiometer (MODIS) on EOS-AM1, *IEEE Trans. Geosci. Remote Sens.*, *36*, 1088–1100.

Bréon, F. M., and S. Colzy (2000), Global distribution of cloud droplet effective radius from POLDER polarization measurements, *Geophys. Res. Lett.*, *27*, 4065–4068.

Buriez, J. C., C. Vanbauce, F. Parol, P. Goloub, M. Herman, B. Bonnel, Y. Fouquart, P. Couvert, and G. Sèze (1997), Cloud detection and derivation of cloud properties from POLDER, *Int. J. Remote Sens.*, *18*, 2785–2813.

Buriez, J. C., M. Doutriaux-Boucher, F. Parol, and N. G. Loeb (2001), Angular variability of the liquid water cloud optical thickness retrieved from ADEOS-POLDER, *J. Atmos. Sci.*, *58*, 3007–3018.

Chambers, L. H., B. A. Wielicki, and N. G. Loeb (2001), Shortwave flux from satellite-measured radiance: A theoretical study over marine boundary layer clouds, *J. Appl. Meteorol.*, *40*, 2144–2162.

C.-Labonnote, L., G. Brogniez, J. F. Gayet, M. Doutriaux-Boucher, and J. C. Buriez (2000), Modeling of light scattering in cirrus clouds with inhomogeneous hexagonal monocrystals. Comparison with in-situ and ADEOS-POLDER measurements, *Geophys. Res. Lett.*, *27*, 113–116.

C.-Labonnote, L., G. Brogniez, M. Doutriaux-Boucher, J. C. Buriez, J. F. Gayet, and H. Chepfer (2001), Polarized light scattering by inhomogeneous hexagonal monocrystals: Validation with ADEOS-POLDER measurements, *J. Geophys. Res.*, *106*, 12,139–12,153.

Coakley, J. A., and P. Chylek (1975), The two-stream approximation in radiative transfer: Including the angle of incident radiation, *J. Atmos. Sci.*, *32*, 409–418.

Cox, C., and W. Munk (1956), Slopes of the sea surface deduced from photographs of the Sun glitter, *Bull. Scripps Inst. Oceanogr.*, *6*, 401–488.

de Haan, J. F., P. B. Bosma, and J. W. Hovenier (1987), The adding method for multiple scattering computations of polarized light, *Astron. Astrophys.*, *183*, 371–391.

Deschamps, P. Y., F. M. Bréon, M. Leroy, A. Podaire, A. Bricaud, J. C. Buriez, and G. Sèze (1994), The POLDER mission: Instrument characteristics and scientific objectives, *IEEE Trans. Geosci. Remote Sens.*, *32*, 598–615.

Deuzé, J. L., P. Goloub, M. Herman, A. Marchand, G. Perry, S. Susana, and D. Tanré (2000), Estimate of the aerosol properties over the ocean with POLDER on ADEOS-1, *J. Geophys. Res.*, *105*, 15,329–15,346.

Diner, D. J., et al. (1998), Multi-angle imaging spectroradiometer (MISR) description and experiment overview, *IEEE Trans. Geosci. Remote Sens.*, *36*, 1072–1087.

Doutriaux-Boucher, M., J.-C. Buriez, G. Brogniez, L. C.-Labonnote, and A. J. Baran (2000), Sensitivity of retrieved POLDER directional cloud optical thickness to various ice particle models, *Geophys. Res. Lett.*, *27*, 109–112.

Dubovik, O., B. Holben, T. F. Eck, A. Smirnov, Y. J. Kaufman, M. D. King, D. Tanré, and I. Slutsker (2002), Variability of absorption and optical properties of key aerosol types observed in worldwide locations, *J. Atmos. Sci.*, *59*, 590–608.

Fougnie, B., P. Y. Deschamps, and R. Frouin (1999), Vicarious calibration of the POLDER ocean color spectral bands using in situ measurements, *IEEE Trans. Geosci. Remote Sens.*, *37*, 1567–1574.

Frouin, R., M. Schwindling, and P. Y. Deschamps (1996), Spectral reflectance of sea foam in the visible and near-infrared: In-situ measurements and remote sensing implications, *J. Geophys. Res.*, *101*, 14,361–14,371.

Han, Q.-Y., W. B. Rossow, and A. A. Lacis (1994), Near-global survey of effective cloud droplet radii in liquid water clouds using ISCCP data, *J. Clim.*, *7*, 465–497.

Hansen, J., G. Russell, D. Rind, P. Stone, A. Lacis, S. Lebedeff, R. Ruedy, and L. Travis (1983), Efficient three-dimensional global models for climatic studies: Models I and II, *Mon. Weather Rev.*, *111*, 609–662.

Hautecoeur, O., and M. Leroy (1998), Surface bidirectional reflectance distribution function observed at global scale by POLDER/ADEOS, *Geophys. Res. Lett.*, *25*, 4197–4200.

Hu, Y. X., B. Wielicki, B. Lin, G. Gibson, S. C. Tsay, K. Stamnes, and T. Wong (2000), A fast and accurate treatment of particle scattering phase functions with weighted singular-value decomposition least squares fitting, *J. Quant. Spectrosc. Radiat. Transfer*, *65*, 681–690.

Kandel, R., et al. (1998), The ScaRaB Earth Radiation Budget dataset, *Bull. Am. Meteorol. Soc.*, *79*, 765–783.

Kaufman, Y. J., D. Tanré, L. Remer, E. F. Vermote, A. Chu, and B. N. Holben (1997), Operational remote sensing of tropospheric aerosol over land from EOS moderate resolution imaging spectroradiometer, *J. Geophys. Res.*, *102*, 17,051–17,068.

Koepke, P. (1984), Effective reflectance of oceanic white caps, *Appl. Opt.*, *23*, 1816–1824.

Loeb, N. G., and J. A. Coakley (1998), Inference of marine stratus cloud optical depths from satellite measurements: Does 1D theory apply?, *J. Clim.*, *11*, 215–233.

Loeb, N. G., F. Parol, J. C. Buriez, and C. Vanbauce (2000), Top-of-atmosphere albedo estimation from angular distribution models using scene identification from satellite cloud property retrievals, *J. Clim.*, *13*, 1269–1285.

Loeb, N. G., N. Manalo-Smith, S. Kato, W. F. Miller, S. K. Gupta, P. Minnis, and B. A. Wielicki (2003), Angular distribution models for top-of-atmosphere radiative flux estimation from the clouds and the Earth's radiant energy system instrument on the tropical rainfall measuring mission satellite. Part I: Methodology, *J. Appl. Meteorol.*, *42*, 240–265.

McFarquhar, G. M., P. Yang, A. Macke, and A. J. Baran (2002), A new parameterization of single-scattering solar radiative properties for tropical anvils using observed ice crystal size and shape distributions, *J. Atmos. Sci.*, *59*, 2458–2478.

Minnis, P., D. P. Garber, D. F. Young, R. F. Arduini, and Y. Takano (1998), Parameterization of reflectance and effective emittance for satellite remote sensing of cloud properties, *J. Atmos. Sci.*, *55*, 3313–3339.

Mishchenko, M. I., I. V. Geogdzhayev, L. Liu, J. A. Ogren, A. A. Lacis, W. B. Rossow, J. W. Hovenier, H. Volten, and O. Muñoz (2003), Aerosol retrievals from AVHRR radiances: Effects of particle nonsphericity and absorption and an updated long-term global climatology of aerosol properties, *J. Quant. Spectrosc. Radiat. Transfer*, *79–80*, 953–972, doi:10.1016/S0022-4073(02)00331-X.

Parol, F., J. C. Buriez, C. Vanbauce, P. Couvert, G. Sèze, P. Goloub, and S. Cheinet (1999), First results of the POLDER "Earth Radiation Budget and Clouds" operational algorithm, *IEEE Trans. Geosci. Remote Sens.*, *37*, 1597–1612.

Poore, K. D., J. Wang, and W. B. Rossow (1995), Cloud layer thickness from a combination of surface and upper-air observations, *J. Clim.*, *8*, 550–558.

Potter, J. F. (1970), The delta function approximation in radiative transfer theory, *J. Atmos. Sci.*, *27*, 943–949.

Riédi, J., P. Goloub, and R. T. Marchand (2001), Comparison of POLDER cloud phase retrievals to active remote sensors measurements at the ARM SGP site, *Geophys. Res. Lett.*, *28*, 2185–2188.

Rossow, W. B., and R. A. Schiffer (1999), Advances in understanding clouds from ISCCP, *Bull. Am. Meteorol. Soc.*, *80*, 2261–2288.

Rossow, W. B., and Y.-C. Zhang (1995), Calculation of surface and top-of-atmosphere radiative fluxes from physical quantities based on ISCCP datasets: 2. Validation and first results, *J. Geophys. Res.*, *100*, 1167–1197.

Sèze, G., C. Vanbauce, J. C. Buriez, F. Parol, and P. Couvert (1999), Cloud cover observed simultaneously from POLDER and METEOSAT, *Phys. Chem. Earth*, *24*, 921–926.

Smirnov, A., B. N. Holben, O. Dubovik, R. Frouin, T. F. Eck, and I. S. Slutsker (2003), Maritime component in aerosol optical models derived from AERONET (Aerosol Robotic Network) data, *J. Geophys. Res.*, *108*(D1), 4033, doi:10.1029/2002JD002701.

Sun, W., N. G. Loeb, and S. Kato (2004), Estimation of instantaneous TOA albedo at 670 nm over ice clouds from POLDER multidirectional measurements, *J. Geophys. Res.*, *109*, D02210, doi:10.1029/2003JD003801.

Suttles, J. T., R. N. Green, P. Minnis, G. L. Smith, W. F. Staylor, B. A. Wielicki, I. J. Walker, D. F. Young, V. R. Taylor, and L. L. Stowe (1988), Angular radiation models for Earth-atmosphere system, *NASA Ref. Publ., RP-1184*, 144 pp.

van de Hulst, H. C. (1980), *Multiple Light Scattering, Tables, Formulas, and Applications*, 739 pp., Elsevier, New York.

Wielicki, B. A., R. D. Cess, M. D. King, D. A. Randall, and E. F. Harrison (1995), Mission to planet Earth: Role of clouds and radiation in climate, *Bull. Am. Meteorol. Soc.*, *76*, 2125–2153.

Wielicki, B. A., et al. (1998), Clouds and the Earth's Radiant Energy System (CERES): Algorithm overview, *IEEE Trans. Geosci. Remote Sens.*, *36*, 1127–1141.

Zhang, Y.-C., W. B. Rossow, and A. A. Lacis (1995), Calculation of surface and top-of-atmosphere radiative fluxes from physical quantities based on ISCCP datasets: 1. Method and sensitivity to input data uncertainties, *J. Geophys. Res.*, *100*, 1149–1165.

J.-C. Buriez, C. Cornet, M. Doutriaux-Boucher, and F. Parol, Laboratoire d'Optique Atmosphérique UMR CNRS 8518, Université des Sciences et Technologies de Lille, F-59655 Villeneuve d'Ascq Cedex, France. (buriez@univ-lille1.fr)